Article

A High–Throughput Molecular Dynamics Study for the Modeling of Cryogenic Solid Formation

Simone Giusepponi [1],*, Francesco Buonocore [1], Massimo Celino [1], Andrea Iaboni [2], Antonio Frattolillo [3] and Silvio Migliori [4]

1   Italian National Agency for New Technologies, Energy and Sustainable Economic Development (ENEA)—C. R. Casaccia, Via Anguillarese 301, 00123 Rome, Italy; francesco.buonocore@enea.it (F.B.); massimo.celino@enea.it (M.C.)
2   MAFE Eni S.p.A., Viale delle Industrie 39, 30175 Venice, Italy; andrea.iaboni@eni.com
3   Italian National Agency for New Technologies, Energy and Sustainable Economic Development (ENEA)—C. R. Frascati, 00044 Frascati, Italy; antonio.frattolillo@enea.it
4   Italian National Agency for New Technologies, Energy and Sustainable Economic Development (ENEA)—Sede Legale, Lungotevere Thaon di Revel 76, 00196 Rome, Italy; ing.silvio.migliori@gmail.com
*   Correspondence: simone.giusepponi@enea.it

Abstract: To predict the favorable thermodynamical conditions and characterize cryogenic pellet formations for applications in nuclear fusion reactors, a high–throughput molecular dynamics study based on a unified framework to simulate the growth process of cryogenic solids (molecular deuterium, neon, argon) under gas pressure have been designed. These elements are used in fusion nuclear plants as fuel materials and to reduce the damage risks for the plasma-facing components in case of a plasma disruption. The unified framework is based on the use of workflows that permit management in HPC facilities, the submission of a massive number of molecular dynamics simulations, and handle huge amounts of data. This simplifies a variety of operations for the user, allowing for significant time savings and efficient organization of the generated data. This approach permits the use of large-scale parallel simulations on supercomputers to reproduce the solid–gas equilibrium curves of cryogenic solids like molecular deuterium, neon, and argon, and to analyze and characterize the reconstructed solid phase in terms of the separation between initial and reconstructed solid slabs, the smoothness of the free surfaces and type of the crystal structure. These properties represent good indicators for the quality of the final materials and provide effective indications regarding the optimal thermodynamical conditions of the growing process.

Keywords: cryogenic solid formation; molecular dynamics simulations; high–throughput; HPC; two-phase system

1. Introduction

In this work, we present a high–throughput molecular dynamics (MD) study based on a unified framework to simulate the growth process of cryogenic solids (molecular deuterium, neon, and argon) under gas pressure to predict and characterize cryogenic pellets for application in a nuclear fusion reactor. These elements are used in fusion nuclear plants as fuel materials and to reduce the damage risks for the plasma-facing components in case of a plasma disruption. In fact, the most effective method for fueling magnetically confined thermonuclear fusion plasmas is the injection of high-speed cryogenic pellets made of frozen hydrogen isotopes. Additionally, the technique of "Shattered Pellet Injection" (SPI), involving the injection of large cryogenic pellets composed of noble gases or their mixtures and shattered into smaller fragments before plasma entry, shows great promise in reducing damage risks for the first wall materials during plasma disruptions. SPI helps distribute plasma energy, mitigate potential damage to in-vessel components, and densify

plasma to suppress runaway electrons and dissipate their energy. To our knowledge, this study represents the first attempt to set up a high–throughput computational framework in the field of the growth of cryogenic solids.

Thus, aided by the use of dedicated workflows that permit management in HPC facilities, the submission of an extensive number of computer calculations, and handle a huge amount of data, we present a high–throughput molecular dynamics study to simulate the growth process of cryogenic solids (molecular deuterium, neon, and argon) under gas pressure, predicting and characterizing the cryogenic pellets for applications in a nuclear fusion reactor. Therefore, this study allows us to reproduce the solid–gas equilibrium curves of these cryogenic solids in good agreement with experimental data. Moreover, the analysis of the reconstructed solid phase permits the characterizations in terms of the separation between initial and reconstructed solid slabs, the smoothness of the free surfaces, and the type of crystal structure. These properties, representing good indicators for the quality of the materials, provide effective indications regarding the optimal thermodynamical conditions of the growing process. In addition to pellets of molecular deuterium used for core fuelling, this method is used to explore the pellet formation of other materials such as neon or argon. These cryogenic pellets are utilized in plasma experiments for impurity and particle transport studies. More recently, two new applications have been identified, one for edge mitigation localized mode and another one for plasma disruption mitigation.

In the following section (Section 2) we present the physical application of our high–throughput study, and then in Section 3, the computational details of the MD simulations based on a unified framework. Finally (Section 4), some physical properties of the cryogenic solids, derived from our high–throughput study, are disclosed.

2. Cryogenic Solid Formation

Cryogenic solids are formed at very extreme conditions of temperature and pressure below the triple point; therefore, they represent a valid example in which computational tools can facilitate and support the experiments that must be carried out using complex experimental equipment. To this aim, a numerical model for the growth of solid light elements (D_2, Ne, and Ar) at cryogenic conditions (very low temperature and pressure) was set up by means of molecular dynamics simulations. This approach is devoted to addressing technological issues related to the production of high-quality pellets for high-speed pipe-gun injectors. The request for intact, high-speed pellets has highlighted several critical issues associated with pellet formation and propulsion.

The pellet formation and propulsion processes taking place in typical pipe-gun injectors can be split up into the following steps:

- The feeding gas (D_2, Ne, or Ar) is introduced into the pipe-gun tube at sub-atmospheric fill pressures.
- A section of the pipe-gun tube, i.e., the active section, is cooled and maintained at temperatures of several degrees below the triple point. This is achieved by means of the thermal contact between the active section of the tube and a metal plaque (oxygen-free copper is typically used due to its high conductivity) that is actively cooled by a cryogenic refrigerator or flowing liquid helium.
- The cooling process leads to the de-sublimation of the fill gas and the growth of solid material on the active section. Good temperature and pressure control during the formation of cryogenic solid is a key factor in determining the final strength of the pellet. Each barrel line is indeed equipped with a pressure controller/flow meter combination that is used to control the freezing pressure and to measure/integrate the mass flow until the desired amount of gas is frozen in each barrel. To ensure that the gas freezes only in the well-defined center cell, upstream and downstream heaters are often used on a single-barrel pipe gun to control the temperature gradients on each side of the zone.
- Before firing, the master heater is typically turned off, and the pellets cool to the minimum possible temperature to have pellets to better withstand the huge stress

during acceleration (one key feature is to have pellets as strong as possible that can survive high acceleration forces, especially for operations with two-stage light gas guns in which these pellets must be accelerated up to few km/s). That temperature is determined by the power of the cryogenic refrigerator and the thermal design of the cryostat and surrounding apparatuses.

- The pellet is finally fired by means of rear propellant gas. High acceleration forces are required to overcome the pellet breakaway pressure. This is the value at which the pellet will instantaneously dislodge because the force exerted on the rear of the pellet exceeds the amount required to overcome the shear stress at the outer surface of the cylindrical pellet. In particular, high breakaway pressures are necessary in the case of Ne and Ar pellets. Propulsion devices must be designed for proper shaping of the propellant pressure pulse to improve pellet acceleration.

Moreover, the pellets must survive inside the curved guiding tubes, with negligible mass and speed losses, and reach the plasma from the high field side (HFS) of the fusion reactor. Injection of intact pellets from the HFS has proved to provide a more effective core particle deposition compared to that from the low field side (LFS). Contrarily, when the quality of the solid material is affected (especially in the case of big pellets) by different freezing conditions, this should lead to intolerable speed limits. Then, the temperature is the key parameter to match since it predominantly dictates the pressure or force required to dislodge solid pellets in a gun barrel. For a detailed analysis of the description of the cryogenic pellet formation and related problems, see Refs. [1–30].

In order to describe and characterize the growth process of the cryogenic pellets by the solidification of gaseous light elements such as D_2, Ne, and Ar, it is necessary to explore the phase transition at very extreme conditions of temperature and pressure below the triple point: T = 18.71 K, P = 171.3 mbar for D_2 [31]; T = 24.556 K, P = 433.70 mbar for Ne [32,33]; T = 83.806 K, P = 688.91 mbar for Ar [32–34]. Then temperatures are below 100 K and pressures are below 700 mbar.

In these ranges of T and P, there are the transition regions of these elements from vapor to solid and vice versa. To have an insight into the physics of these materials in these conditions, an atomistic model can be a very useful method; an atomic model based on extensive classical molecular dynamics simulations is required since systems are constituted by hundreds of thousands of particles.

We investigated the de-sublimation process in which gaseous D_2, Ne, and Ar, solidify on a surface and then the reconstructed solids were characterized. We calculated the absorption rates and the equilibrium temperature and pressure. Next, the solid–vapor equilibrium curves are reconstructed with good agreement with experimental results. Moreover, slabs and surfaces are described considering the separation between initial and reconstructed solid slabs, the roughness of the reconstructed free surfaces, and the fraction of particles in FCC lattice positions. These properties are also of interest to provide insight into the parameters useful to improve the quality of the solids. In this work, the method presented in our previous work in which we characterized the growth of molecular deuterium at the pressure of 25 mbar [35] is extended to a wider range of pressure and to other cryogenic solids.

3. Computational Details

In order to model the cryogenic solids formation, which requires systems with thousands of particles, the classical molecular dynamics methods are adopted using the LAMMPS (Large-scale Atomic/Molecular Massively Parallel Simulator) code [36,37]. Classical molecular dynamics simulations have become a very valuable tool for the investigation of atomic and molecular systems, mainly in the area of materials science and molecular biophysics (for a wider description of the method including also its limitations or potential source of errors, see Refs. [38–43]). Molecular dynamics methods are based on the integration of Newton's equations of a system of interacting particles via a potential energy. The potential energy can be approximated by an "effective" pair potential that gives a

remarkably good description of the material properties because the average n-body terms are included. This has the great advantage of avoiding the calculations of n-body term interactions that are very time-consuming on a computer. However, MD simulations must be used with an awareness of a proper choice of the numerical parameters suitable for the specific material undergoing specific thermodynamic conditions.

We simulated both one-phase and two-phase systems in ranges of T and P, from 0 K and 0 mbar, up to T and P near the D_2, Ne, and Ar triple points. To model the interaction between particles the Lennard–Jones (LJ) and Mie potentials were used. For D_2, LJ potential with ε = 2.29 meV and σ = 3.07 Å [35,44]; for Ne, LJ potential with ε = 3.02468 meV and σ = 2.72 Å [45]; for Ar 13-6 Mie potential with ε = 10.52 meV and σ = 3.405 Å [46]. The LJ potential and its generalization Mie potential are simple, idealized pair potentials, widely and historically used in computer simulations, since they provide a reasonable description of the properties of noble gasses. Subsequently, different approaches have been proposed considering for example semiempirical potentials and ab initio potentials, even if the latter are computationally very expensive. For a more detailed discussion of these potentials, their strength, and limitations see Refs. [47–54]. Having to simulate thousands of particles across a wide range of thermodynamic conditions for extended periods, we opted for LJ and Mie potentials. These potentials provide reliable results for this class of materials, are tested and commonly used, and are less computationally demanding.

To perform molecular dynamics simulations both pressure and temperature are controlled by the Berendsen barostat and thermostat [55], while constant NVE integration was used to update particles positions and velocities. A timestep as small as t_s = 0.001 ps is implemented to accurately integrate equations of motion. Periodic boundary conditions (PBC) were imposed to mimic an infinitely extended system in the x, y, and z directions. The numerical model consists of a slab of solid material composed of N = 64,000 particles forming a crystalline FCC bulk (40 × 40 × 10 crystal unit cells) coupled with a gas phase system of 64,000 particles, with 128,000 particles in total. Before the simulation of the two-phase systems (slab + gas), one-phase systems (solid, slab, and gas) were checked and analyzed. The energy minimization of the bulk solid systems at T = 0 K, yields the following values for the lattice parameter and the cohesion energy: for D_2, a_0 = 4.75 Å (exp. 5.07 Å [56]) and E_{coes} = 19 meV/particle; for Ne, a_0 = 4.20 Å and E_{coes} = 25.49 meV/atom (exp. 4.42 Å and 26.12 meV/atom [57]); for Ar a_0 = 5.25 Å (exp. 5.31 Å [58]) and E_{coes} = 87.40 meV/atom. Therefore, in the two-phase system, the initial configuration is made of a slab of solid material with a size of about 200 × 200 × 50 Å^3 for D_2, 170 × 170 × 45 Å^3 for Ne and 215 × 215 × 55 Å^3 for Ar, coupled with a gas system with same size in x and y directions and size in z direction in the order of 10^6 Å in order to have the desired temperature and pressure conditions. The final configuration of the reconstructed solid is reached when there is an increase of +75% in the thickness of the slab (size of about 200 × 200 × 90 Å^3 for D_2, 170 × 170 × 80 Å^3 for Ne and 215 × 215 × 100 Å^3 for Ar). This permits solid slabs thick enough to analyze the growth and crystal structure, and free surfaces wide enough to characterize their roughness. Moreover, because for each value of T and P, the produced data range from tens up to hundreds of GBytes, this is a trade-off between the size of the systems and the storage capacity of the computational infrastructure. In fact, some test calculations were performed for wider systems with 6.4 M (solid) + 6.4 M (gas) particles and longer time. Requiring more computational resources, these simulations were executed on the Summit system at Oak Ridge National Laboratory using the four workflows. This allowed for testing the functionality workflows also in another HPC infrastructure. However, these calculations yielded the same T-P solid–gas curves but with very large data files produced (up to hundreds of TBytes for each T and P value) making their management overwhelming.

The crystalline phase model was characterized by heating the system from T = 0 K up to 30 K (for D_2), 40 K (for Ne), and 100 K (for Ar) by executing MD simulations at constant pressure P = 0 mbar. Every run lasts 1000 ps: the temperature-raising process involves the first 200 ps, followed by 800 ps in which the system is thermalized at the

target temperature (see Figure 1). Physical quantities (density, energies per particle, size of the simulation cell, temperature, pressure, and tensor pressure) are computed and monitored during the simulations, moreover, their mean values and standard deviations were calculated over the last 500 ps of simulation in which also the radial pair correlation function g(r) was computed. This ensures that the systems have reached their equilibrium and provide sufficiently accurate estimates. Figure 1 depicts the heating sequence of the molecular deuterium and in the insets, the trends of the physical quantities for the increase in temperature from T = 4 to 5 K. Highlighted in red are the range of time in which mean values and deviation standards are computed.
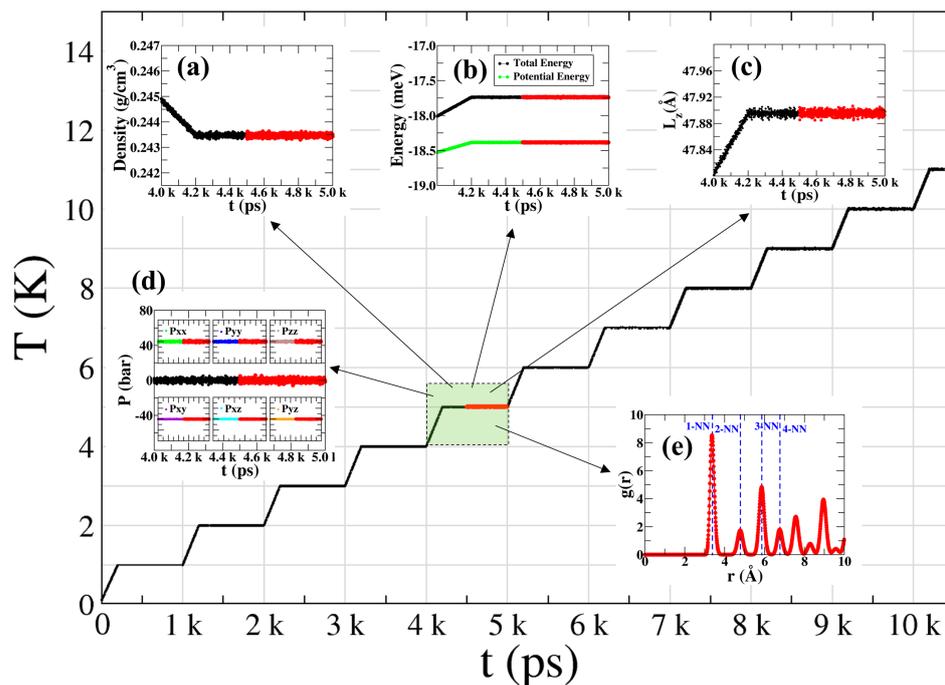
Figure 1. Trend of the temperature for the heating process of the solid molecular deuterium: every run simulates 1000 ps: the first 200 ps were used to raise the temperature of the system, and the following 800 ps were used to thermalize it at the target temperature. In the insets the trends of the physical quantities for the increase from T = 4 to 5 K: (**a**) density, (**b**) total and potential energies for particle, (**c**) size (z-dimension) of the simulation cell, (**d**) pressure and tensor stress, and (**e**) radial pair correlation function with distance of the nearest-neighbor (NN). Highlighted in red are the time intervals in which mean values and standard deviations are calculated.

To generate the slabs, the obtained relaxed solids at T = 0 were cut along the (001) Miller plane and the simulation cells were extended orthogonally to the surface to have a void region of about 150 Å. Thanks to PBC, an infinitely solid slab with two free surfaces perpendicular to the z direction is modeled. The solid slabs underwent the same thermal treatment imposing zero pressure along the x and y directions ($P_x = P_y = 0$ mbar).

The gas phase systems were prepared starting from n = 64,000 particles randomly placed in a tetragonal simulation cell in which $L_x = L_y$ equals the corresponding dimensions of the solid slabs and L_z calculated from the ideal gas equation at the desired temperature and pressure conditions. The gas systems were equilibrated for 1000 ps by NPT-MD, in which $L_x = L_y$ were kept fixed, and L_z is free to vary. In the cooling process, the final configurations of the system were used as the first configurations for the successive simulation at a decreased value of T. As already completed for the bulk and slab solids, each run lasts 1000 ps; 200 ps to decrease the temperature followed by 800 ps to thermalize the system. To check the thermalization process, the last 500 ps of each run were used to perform a statistical analysis, that confirmed that all the simulated systems are always well equilibrated. Figure 2 depicts the cooling sequence of the neon gas, in the insets the

trends of the physical quantities for the decreasing in temperature from T = 36 to 35 K. Highlighted in red are the time intervals in which mean values and standard deviations are calculated.
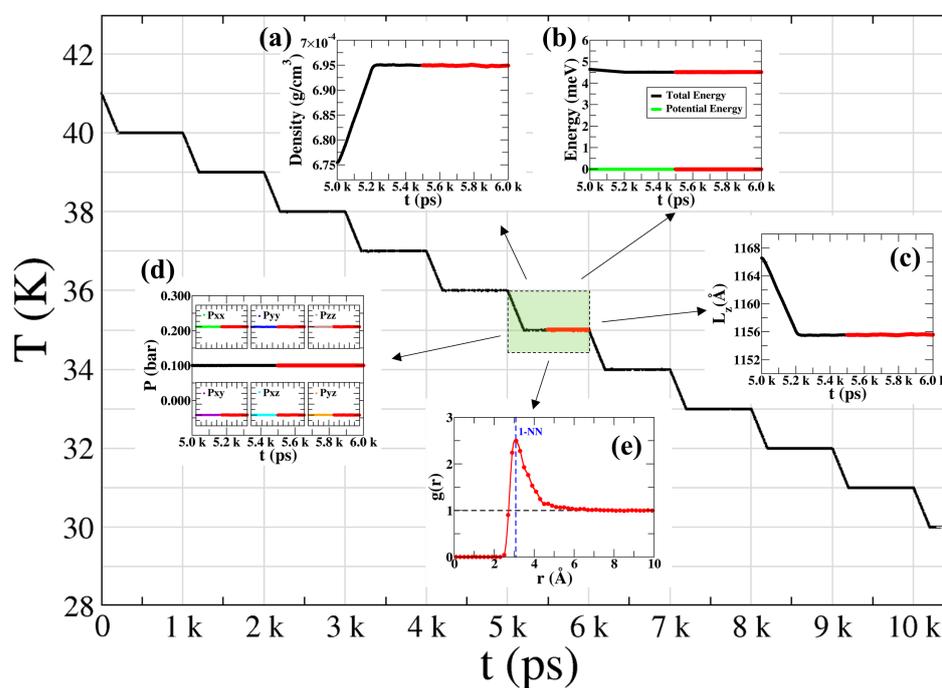
Figure 2. Trend of the temperature for the cooling process of the neon gas: every run simulates 1000 ps: the first 200 ps were used to lower the temperature of the system, and the following 800 ps were used to thermalize it at the target temperature. In the insets the trends of the physical quantities for the decreasing from T = 36 to 35 K: (**a**) density, (**b**) total and potential energies for atom, (**c**) size (z-dimension) of the simulation cell, (**d**) pressure and tensor stress, (**e**) radial pair correlation function with distance of the first nearest-neighbor (1-NN). In red, the range of time in which mean values and deviation standards are computed is highlighted.

The solid–gas interface (two-phase system) at pressure P = P* and in the range of temperature as reported in Table 1 is formed by coupling the solid slabs and the gas systems previously prepared (one-phase systems). A slab of solid that exposes two free surfaces (orthogonal to the z direction) to a gas of the same material represents the starting configuration. To permit both systems to interact gradually, an initial distance of 100 Å is inserted between the two phases. The systems are infinitely extended in the x and y directions thanks to PBC. Cryogenic pellets are formed by solidifying gaseous light elements with T and P below those of the triple point. By imposing the pressure in the z direction at P* and 0 mbar in the x and y directions, the evolution of the two-phase systems was investigated by executing a set of MD simulations for different values of the temperature T*. The solid and gas phases were thermalized with two Berendsen thermostats with different temperature-damping parameters (lower values for the solids and higher values for the gasses). This permits the temperature of the two phases to be controlled separately, taking into account the different heat transfer conditions between solid and gas.

To deal with a huge number of MD simulations (in the order of tens of thousands) that span different thermodynamic conditions for one-phase systems (solids, slabs, gas) and two-phase systems (solid–gas interfaces) for the three elements (D_2, Ne, Ar), four different workflows (WFs) implemented in Python code were set up. These are numerical simulations with dependencies that must be executed and managed over long time periods in which failure tracking, recovery, and provenance are important to ensure that all tasks are executed correctly. These calculations must be executed in an HPC infrastructure with a batch scheduler that is designed to perform small numbers of massively parallel

simulations rather than very large numbers of smaller tasks (all the MD simulation runs were submitted to the ENEAGRID CRESCO6 cluster using the LAMMPS code parallel version compiled with intel/intelmpi. CRESCO6 (1400 Tflops peak), is equipped with 434 nodes, each with 2×24 cores Intel Xeon Platinum 8160 CPU @2.1 GHz (Intel, Santa Clara, CA, USA); 192 GB RAM and interconnected with Intel Omni-Path 100 GB/s. IBM/LSF is the resource manager with a 24 h maximum duration for the execution of the jobs). The adoption of these workflows saves the user a lot of time because this avoids a series of actions, checks, and file manipulations at the end of each MD simulation run. For example, to set up the simulation, the following operations are required of the user: creation of the working directory and subdirectory to store files of interest; preparation of the input file and submission of the job to the HPC facility; check if the job finished properly and if all the desired files were correctly produced; extraction of the physical quantities of interest from the output files and plotting of them to inspect their trends; and so on, repeating subsequently these operations until the desired result is reached. Another advantage is that WFs can be launched in parallel generating a flow of workflows with further saving of time (the four workflows, WF4gas, WF4interface, WF4slab, and WF4solid, are collected in a GitLab project called CryoMatPy and are distributed as Python libraries that can be downloaded from https://gitlab.brindisi.enea.it/simone.giusepponi1/cryomatpy (accessed on 30 April 2024)).

Table 1. List of the elements with the corresponding values of the triple points. Pressure and temperature ranges for the one-phase systems (solid, slab, gas) and for two-phase systems (slab + gas).

Element	Triple Point P (mbar) T (K)	Solid P (mbar) T Range (K)	Slab $P_x = P_y$ (mbar) T Range (K)	Gas P (mbar) T Range (K)	Two-Phase P_z (mbar) T Range (K)
D_2	171.3 18.71	0 0–30	0 0–30	5, 10, 15, 20, 25 30–5	5, 10, 15, 20, 25 5–20
Ne	433.70 24.556	0 0–40	0 0–40	10, 25, 50, 100 45–5	10, 25, 50, 100 8–22
Ar	688.91 80.806	0 0–90	0 0–90	25, 50, 100, 250, 500 100–15	25, 50, 100, 250, 500 20–80

4. Results and Discussion

4.1. T-P Solid–Gas Curves

In Figure 3 we show the main physical result achieved: the T-P diagram phase for (a) molecular deuterium, (b) neon, and (c) argon. Red symbols refer to experimental works [21]. Blue and orange symbols refer to T and P values in which MD simulations evolve to the solid or gas phase, respectively. The grey bars represent the range in which we can estimate the solid–gas equilibrium point by using the simulations. We observe an agreement between experimental and numerical results for molecular deuterium, even if the predicted values from the MD seem to be slightly underestimated. The agreement is excellent for neon and even more for argon, in fact, experimental values of the vapor pressure are in the middle between blue (solid) and orange (gas) symbols. This may be due to the fact that for neon and argon, there are lower quantum effects, and the LJ and Mie potentials better reproduce the interactions between particles compared to deuterium. Although we reached a good level of accuracy in the estimate of equilibrium points, further simulations are in progress to provide more accurate values and specific works are in preparation for the three elements (D_2, Ne, Ar).
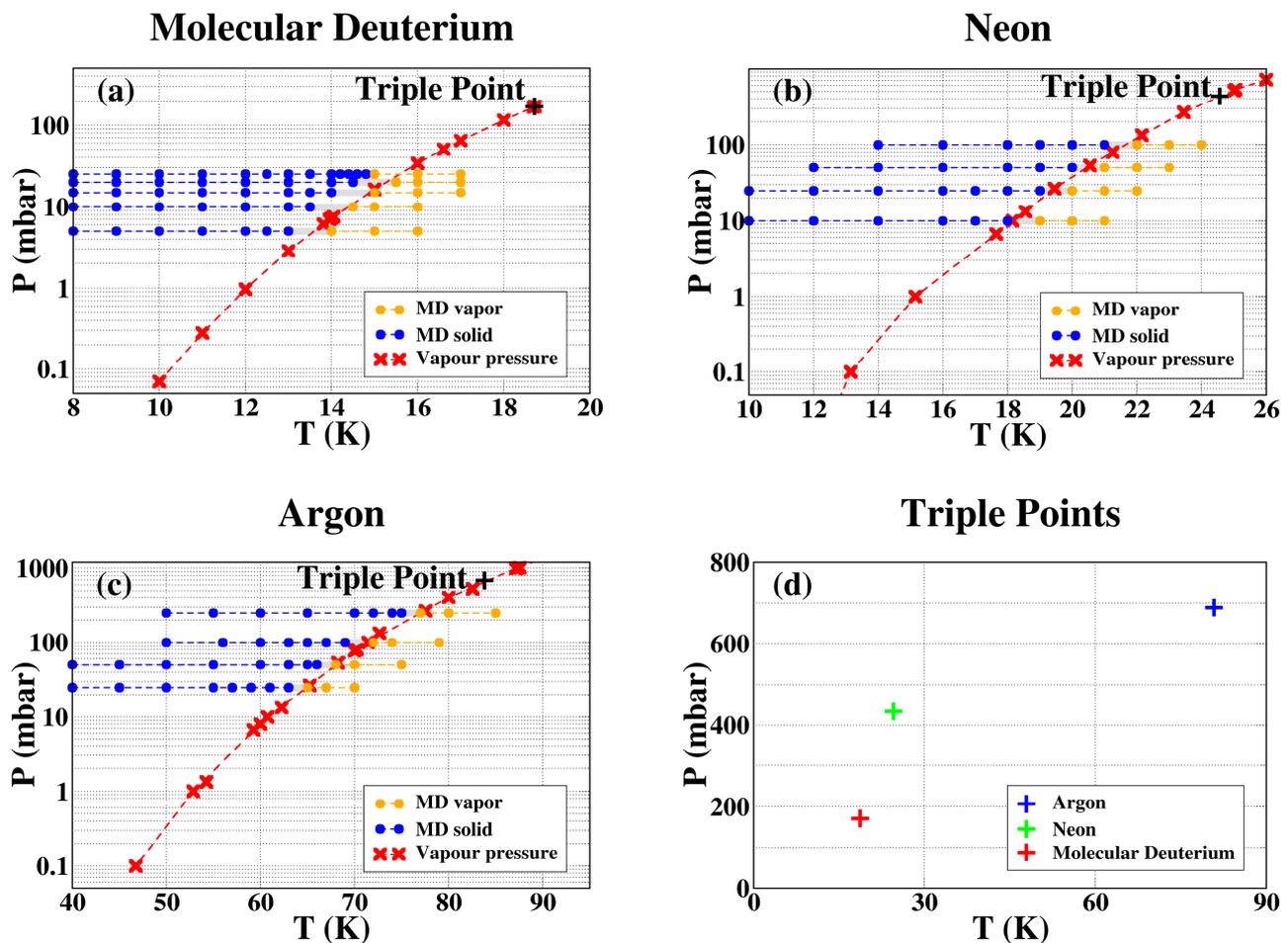
Figure 3. Equilibrium solid–gas curves for (**a**) molecular deuterium, (**b**) neon, and (**c**) argon. Black symbol refers to triple point. Red symbols refer to experimental values. Blue/orange symbols refer to the MD simulations that evolve to the solid–gas phase. The lines connecting the points are for guidance only. (**d**) Triple points of the three elements reported in P-T linear scale plot.

4.2. Surface Characterization

An important aspect of performing theoretical calculations and numerical simulations is an extended knowledge of material properties in a PT domain not yet reached in experiments. In the following, we report some examples of reconstructed cryogenic solids and their characterization. For each of the three systems (D_2, Ne, and Ar), the highest and the lowest values of pressure were chosen (see Figure 3), and for each P value, three values of temperatures were selected.

1. For molecular deuterium:
   - P = 5 mbar and T = 8, 10, and 12.5 K (see Figure 4 left side);
   - P = 25 mbar and T = 9, 12, and 14.6 K (see Figure 4 right side).
2. For neon:
   - P = 10 mbar and T = 10, 12, and 16 K (see Figure 5 left side);
   - P = 100 mbar and T = 12, 16, and 21 K (see Figure 5 right side).
3. For argon:
   - P = 25 mbar and T = 45, 55, and 61 K (see Figure 6 left side);
   - P = 250 mbar and T = 50, 65, and 74 K (see Figure 6 right side).
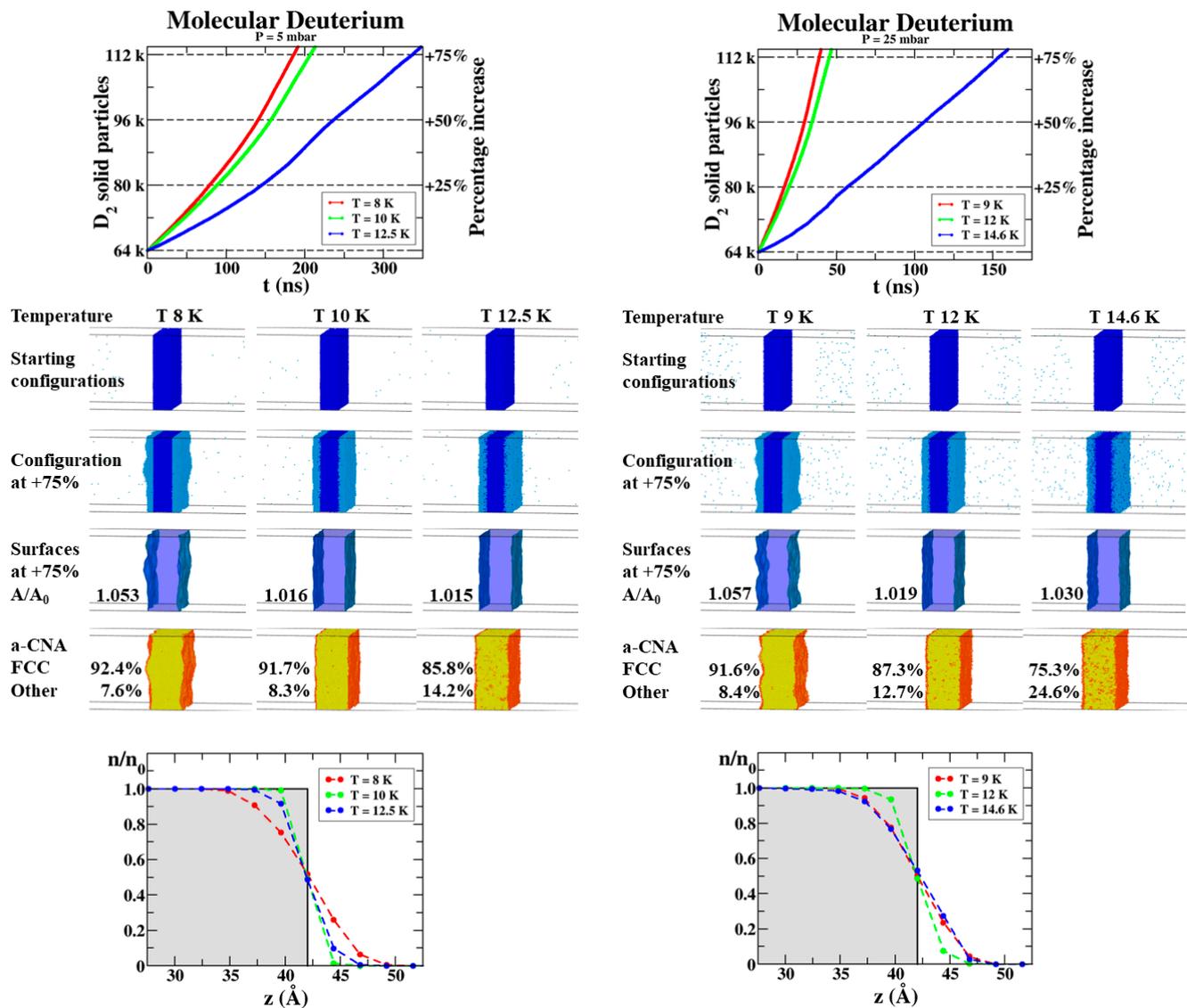
Figure 4. Characterizations of reconstructed molecular deuterium at P = 5 mbar and T = 8, 10, and 12.5 K (**left side**) and P = 25 mbar and T = 9, 12, 14.6 K (**right side**). Graphs on the top report the number of particles (left vertical axis) in solid phase and their increment (right vertical axis) during the MD simulations. In the middle, snapshots of the starting configuration and the configuration at the 75% increment of solid phase (particles that initially were in solid phase are in dark blue, whereas those initially in gas phase are in light blue). Surface profiles of the reconstructed solid (at +75%) and the ratio between their area A compared to the ideal ones A_0. Local structural environment (at +75%) and percentage of particles in FCC crystalline structure (in yellow). Graphs at bottom show the distribution of solid particles (at +75%) along z direction compared to the ideal case of step function (shadowed area).

The graphs on the top of each figure (Figures 4–6) report the number of solid particles during the simulation. There are different absorption rates depending on the element and on the thermodynamic conditions. The closer is T to the equilibrium value, the slower the rate of solid growth. In the limit of $T = T_e$, the solid and gas phases balance each other, and the absorption rate vanishes. After an initial transient, the number of solid particles increases almost linearly with time especially in the central and final part of the simulations when the increment rises from 25 to 75%. This permits evaluating and comparing the absorption rate at different thermodynamic conditions of P and T.
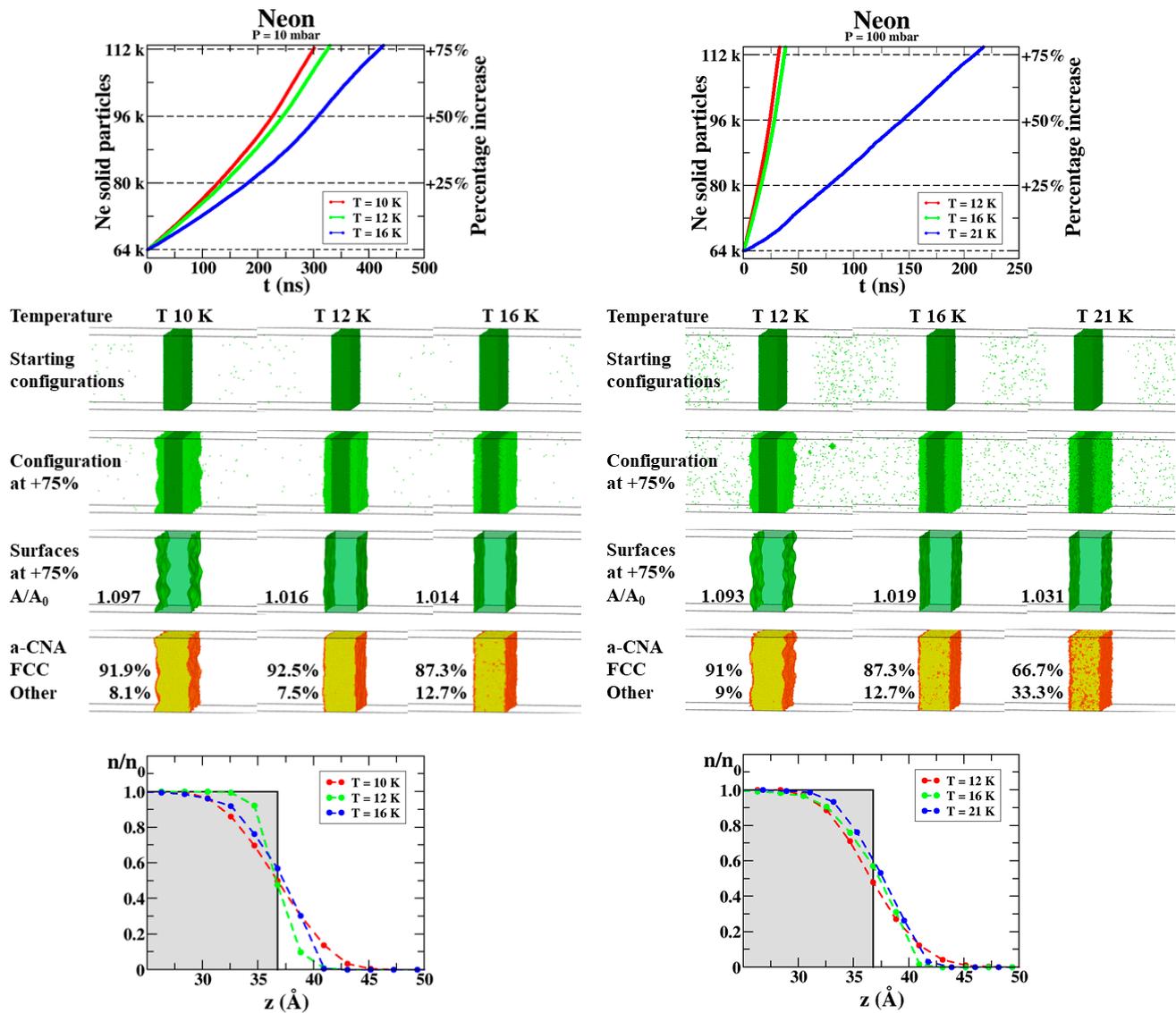
Figure 5. Characterizations of reconstructed neon at P = 10 mbar and T = 10, 12, and 16 K (**left side**) and P = 100 mbar and T = 12, 16, 21 K (**right side**). Graphs on the top report the number of particles (left vertical axis) in solid phase and their increment (right vertical axis) during the MD simulations. In the middle, snapshots of the starting configuration and the configuration at the 75% increment of solid phase (particles that initially were in solid phase are in dark green, whereas those initially in gas phase are in light green). Surface profiles of the reconstructed solid (at +75%) and the ratio between their area A compared to the ideal ones A_0. Local structural environment (at +75%) and percentage of particles in FCC crystalline structure (in yellow). Graphs at bottom show the distribution of solid particles (at +75%) along z direction compared to the ideal case of step function (shadowed area).

　　　The snapshots show the starting configurations and the configurations at the 75% increment of the solid phase. Particles that were initially in the solid phase are depicted in dark colors, whereas those that were initially in the gas phase are shown in light colors (dark and light blue for D_2, dark a light green for Ne, and dark and light red for Ar). This distinction permits us to highlight how clear is the separation between dark- and light-colored particles. The lower the temperature, the sharper the separation between particles. On the contrary, as the T increases to approach T_e, the sublimation process begins to be competitive with that of de-sublimation with a consequent mixing between particles and a lower clear separation between them.
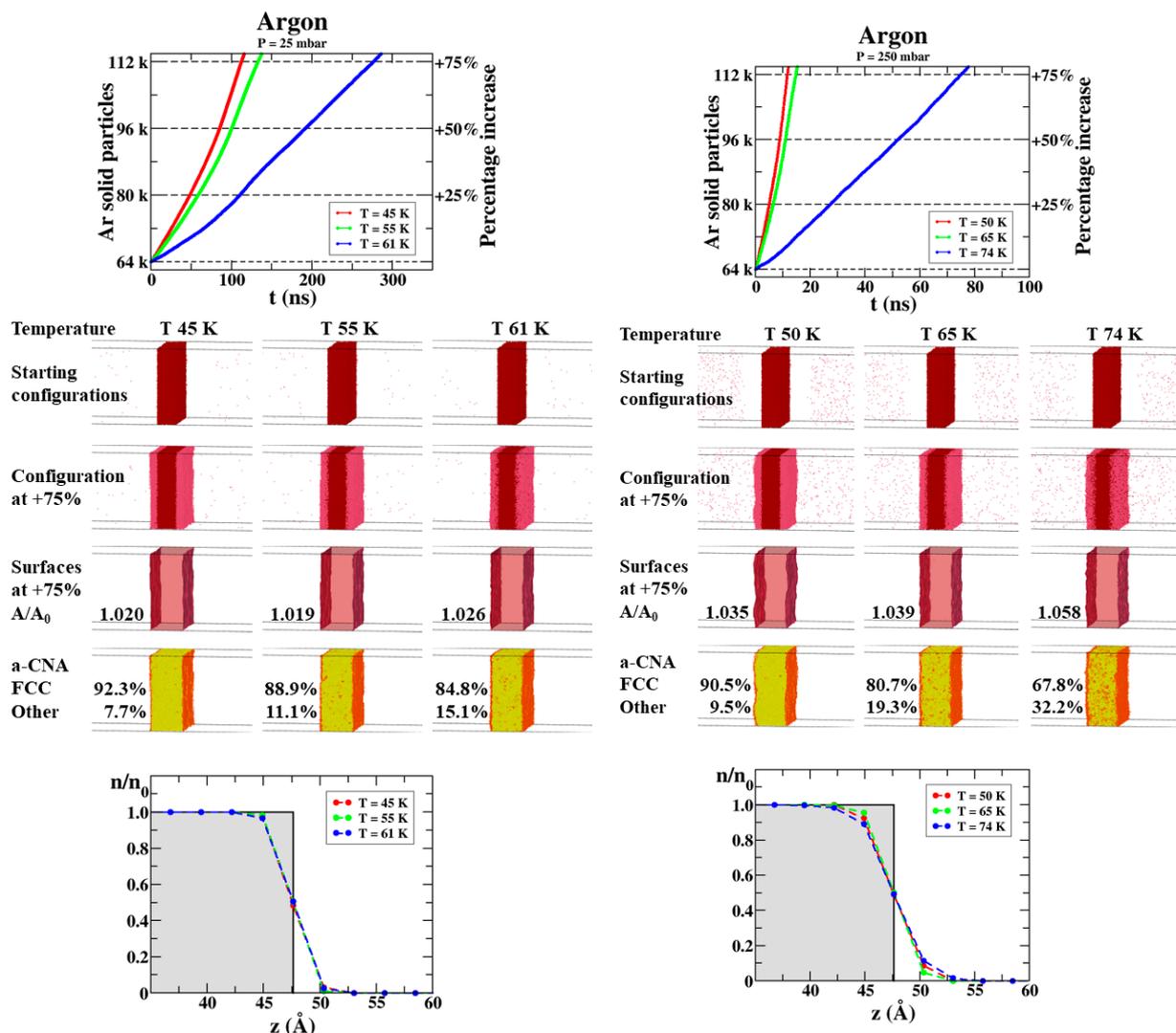
Figure 6. Characterizations of reconstructed argon at P = 25 mbar and T = 45, 55, and 61 K (**left side**) and P = 250 mbar and T = 50, 65, and 74 K (**right side**). Graphs on the top report the number of particles (left vertical axis) in solid phase and their increment (right vertical axis) during the MD simulations. In the middle, snapshots of the starting configuration and the configuration at the 75% increment of solid phase (particles that initially were in solid phase are in dark red, whereas those initially in gas phase are in light red). Surface profiles of the reconstructed solid (at +75%) and the ratio between their area A compared to the ideal ones A_0. Local structural environment (at +75%) and percentage of particles in FCC crystalline structure (in yellow). Graphs at bottom show the distribution of solid particles (at +75%) along z direction compared to the ideal case of step function (shadowed area).

Another aspect to take into consideration is how to evaluate the roughness of the reconstructed solid. This is highlighted in the middle of the three figures (Figures 4–6) in which the free surfaces of the solid slabs (at the increment of 75% of the solid phase) are depicted and values of the ratio A/A_0 are reported. A is the area of the free surfaces and A_0 is the area of the "ideal" free surfaces of side L_x and L_y, that is completely flat [59]. A ratio A/A_0 close to the unity, indicates a flat surface, as the ideal one, whereas values that deviate from the unit denote coarse surfaces. In particular, this occurs at very low T, when the sublimation process is very fast giving rise to very corrugated surfaces with a coarse granularity, or for higher temperatures close to the equilibrium ones, when the particles having increased mobility between the solid and the gas phases produce a "fluid" solid with wavy surfaces and fine granularity.

Moreover, to evaluate the "order" of the reconstructed solid, we inspected the local structural environment of the atoms using the adaptive common neighbor analysis (a-CNA) [60]. All three elements (D_2, Ne, and Ar) have FCC crystalline structures. In the figures, snapshots of the reconstructed solid are shown coloring each particle according to its structural environment: yellow denotes FCC (face-cantered cubic), green HCP (hexagonal close-packed), blue BCC (body-cantered cubic), red icosahedral, and orange unknown coordination structure. It also reported the percentage of the particles in FCC crystalline structures at different temperatures.

Finally, to further characterize the reconstructed solid and its free surfaces, in the bottom graphs of the figures, we consider the distribution of solid particles along the z direction at the increment of +75%. In the graphs, it is reported the normalized number of solid particles, n/n_0 versus their z coordinate compared to the ideal case of a step function (perfectly flat surface). The curves refer to the temperature indicated in the insets. In general, it is observed that for the intermediate value of T the surface is more similar to the ideal one, confirming that for values of temperature too low or too close to the equilibrium ones, the reconstructed solid and surfaces are less regular.

5. Conclusions

In conclusion, we presented a high–throughput molecular dynamic study based on a unified framework to simulate the growth process of cryogenic solids (molecular deuterium, neon, and argon) under gas pressure to predict and characterize cryogenic pellets for applications in nuclear fusion reactors. To reach this goal, workflows were set up to have a unified framework for managing the submission of a massive number of molecular dynamics simulations in HPC facilities and handling huge amounts of data. The workflows relieve users of a series of repetitive actions, including the preparation, submission, and verification of MD simulations, as well as the subsequent manipulation of generated data files. This results in significant time savings and ensures that data are organized properly. This study allowed us to reproduce the solid–gas equilibrium curves of cryogenic solids like molecular deuterium, neon, and argon, and to analyze and characterize the reconstructed solid phase in terms of the separation between initial and reconstructed solid slabs, the smoothness of the free surfaces and the type of the crystal structure. These properties represent good indicators for the quality of the materials and provide effective indications regarding the optimal thermodynamical conditions of the growing process. Moreover, our unified framework can be used for the study of other cryogenic materials and their mixtures.

Author Contributions: Conceptualization, S.M. and A.F.; methodology, S.G., F.B. and M.C.; software, F.B. and S.G.; validation, S.M. and A.F.; formal analysis, S.G., F.B. and M.C.; investigation, S.G., F.B. and M.C.; data curation, S.G. and F.B.; writing—original draft preparation, S.G.; writing—review and editing, A.I., M.C., F.B. and S.M.; visualization, S.G.; supervision, M.C., S.M. and A.F. All authors have read and agreed to the published version of the manuscript.

Data Availability Statement: The original contributions presented in the study are included in the article, further inquiries can be directed to the corresponding author/s.

Conflicts of Interest: The authors declare no conflicts of interest.

References

1. Combs, S.K.; Milora, S.L.; Foust, C.R. Simple pipe gun for hydrogen pellet injection. *Rev. Sci. Instrum.* **1986**, *57*, 2636–2637. [CrossRef]
2. Sørensen, H.; Nordskov, A.; Sass, B.; Visler, T. Simplified pipe gun. *Rev. Sci. Instrum.* **1987**, *58*, 2336. [CrossRef]
3. Reggiori, A.; Carlevaro, R.; Riva, G.; Daminelli, G.B.; Scaramuzzi, F.; Frattolillo, A.; Martinis, L.; Cardoni, P.; Mori, L. High-speed pellet injection with a two-stage pneumatic gun. *J. Vac. Sci. Technol. A* **1988**, *6*, 2556–2558. [CrossRef]
4. Lang, P.T.; Büchl, K.; Kaufmann, M.; Lang, R.S.; Mertens, V.; Müller, H.W.; Neuhauser, J.; Upgrade, A.; Teams, N. High-Efficiency Plasma Refuelling by Pellet Injection from the Magnetic High-Field Side into ASDEX Upgrade. *Phys. Rev. Lett.* **1997**, *79*, 1487–1490. [CrossRef]
5. Viniar, I.; Reznichenko, P.; Lukin, A.; Umov, A.; Sudo, S. Hydrogen-encapsulated impurity pellet injector for plasma diagnostics. *Rev. Sci. Instrum.* **2001**, *72*, 2575–2578. [CrossRef]
6. Pautasso, G.; Tichmann, C.; Egorov, S.; Zehetbauer, T.; Gruber, O.; Maraschek, M.; Mast, K.-F.; Mertens, V.; Perchermeier, I.; Raupp, G.; et al. On-line prediction and mitigation of disruptions in ASDEX Upgrade. *Nucl. Fusion* **2002**, *42*, 100–108. [CrossRef]
7. Lorenz, A.; Combs, S.; Reich, M.; Lang, P.; Watson, M.; Wilson, D.; Wittmann, C. Mass transfer in long pellet guiding systems at ASDEX upgrade and JET. *Fusion Eng. Des.* **2003**, *69*, 15–20. [CrossRef]
8. Cannas, B.; Fanni, A.; Marongiu, E.; Sonato, P. Disruption forecasting at JET using neural networks. *Nucl. Fusion* **2004**, *44*, 68–76. [CrossRef]
9. Combs, S.; Baylor, L.; Caughman, J.; Fehling, D.; Foust, C.; Jernigan, T.; Maruyama, S.; McGill, J.; Rasmussen, D.; Ridenour, J.; et al. Pellet delivery and survivability through curved guide tubes for fusion fueling and its implications for ITER. *Fusion Eng. Des.* **2005**, *75–79*, 691–696. [CrossRef]
10. Pégourié, B.; Waller, V.; Dumont, R.J.; Eriksson, L.-G.; Garzotti, L.; Géraud, A.; Imbeaux, F. Modelling of pellet ablation in additionally heated plasmas. *Plasma Phys. Control. Fusion* **2005**, *47*, 17–35. [CrossRef]
11. Baylor, L.; Jernigan, T.; Parks, P.; Antar, G.; Brooks, N.; Combs, S.; Fehling, D.; Foust, C.; Houlberg, W.; Schmidt, G. Comparison of deuterium pellet injection from different locations on the DIII-D tokamak. *Nucl. Fusion* **2007**, *47*, 1598–1606. [CrossRef]
12. Pégourié, B.; Waller, V.; Nehme, H.; Garzotti, L.; Géraud, A. Homogenization of the pellet ablated material in tokamaks taking into account the ∇B-induced drift. *Nucl. Fusion* **2006**, *47*, 44–56. [CrossRef]
13. Baylor, L.; Combs, S.; Foust, C.; Jernigan, T.; Meitner, S.; Parks, P.; Caughman, J.; Fehling, D.; Maruyama, S.; Qualls, A.; et al. Pellet fuelling, ELM pacing and disruption mitigation technology development for ITER. *Nucl. Fusion* **2009**, *49*, 085013. [CrossRef]
14. Combs, S.K.; Meitner, S.J.; Baylor, L.R.; Caughman, J.B.; Commaux, N.; Fehling, D.T.; Foust, C.R.; Jernigan, T.C.; McGill, J.M.; Parks, P.B.; et al. Alternative techniques for injecting massive quantities of has for plasma-disruption mitigation. *IEEE Trans. Plasma Sci.* **2010**, *38*, 400. [CrossRef]
15. Lang, P.T.; Day, C.; Fable, E.; Igitkhanov, Y.; Köchl, F.; Mooney, R.; Pegourie, B.; Ploeckl, B.; Wenninger, R.; Zohm, H. Considerations on the DEMO pellet fueling system. *Fusion Eng. Des.* **2015**, *96–97*, 123–128. [CrossRef]
16. Pégourié, B.; Day, C.; Frattolillo, A.; Koechl, F.; Lang, P.T. Physical constraints on the design of the DEMO pellet fueling system. In Proceedings of the 43rd EPS Conference on Plasma Physics, Leuven, Bergium, 4–8 July 2016; p. 4.076.
17. Frattolillo, A.; Bombarda, F.; Day, C.; Lang, P.; Migliori, S.; Pégourié, B. An innovative approach for DEMO core fuelling by inboard injection of high-speed pellets. *Fusion Eng. Des.* **2017**, *124*, 846–849. [CrossRef]
18. Meitner, S.; Baylor, L.; Commaux, N.; Shiraki, D.; Combs, S.; Bjorholm, T.; Ha, T.; McGinnis, W. Design and Commissioning of a Three-Barrel Shattered Pellet Injector for DIII-D Disruption Mitigation Studies. *Fusion Sci. Technol.* **2017**, *72*, 318. [CrossRef]
19. Frattolillo, A.; Baylor, L.R.; Bombarda, F.; Combs, S.K.; Day, C.; Lang, P.T.; Migliori, S.; Pegourie, B.; Ploeckl, B. Core Fueling of DEMO by Direct Line Injection of High-Speed Pellets From the HFS. *IEEE Trans. Plasma Sci.* **2018**, *46*, 1429–1435. [CrossRef]
20. Combs, S.K.; Baylor, L.R. Pellet-Injector Technology—Brief History and Key Developments in the Last 25 Years. *Fusion Sci. Technol.* **2017**, *73*, 493–518. [CrossRef]
21. Baylor, L.R.; Meitner, S.J.; Gebhart, T.; Caughman, J.B.O.; Herfindal, J.L.; Shiraki, D.; Youchison, D.L. Shattered pellet injection technology design and characterization for disruption mitigation experiments. *Nucl. Fusion* **2019**, *59*, 066008. [CrossRef]
22. Meitner, S.J.; Baylor, L.R.; Gebhart, T.E.; Harris, J.H.; Mcginnis, W.D.; Bjorholm, T.P.; Logan, K.G. Design of a Continuous Pellet Fueling System for Wendelstein 7-X. *IEEE Trans. Plasma Sci.* **2019**, *48*, 1585–1590. [CrossRef]
23. Gebhart, T.E.; Ghiozzi, A.G.; Velez, D.A.; Baylor, L.R.; Chilen, C.; Meitner, S.J. Shear Strength and Release of Large Cryogenic Pellets from the Barrel of a Shattered Pellet Injector for Disruption Mitigation. *Fusion Sci. Technol.* **2021**, *77*, 721–727. [CrossRef]
24. Baylor, L.R.; Meitner, S.J.; Gebhart, T.E.; Lang, P.T.; Ploeckl, B. Issues in Formation of Cryogenic Pellets for Fusion Applications. *Fusion Sci. Technol.* **2021**, *77*, 728–737. [CrossRef]
25. Meitner, S.J.; Baylor, L.R.; McGinnis, W.D. R&D Extruder Developments for the Wendelstein 7-X Continuous Pellet Fueling System. *IEEE Trans. Plasma Sci.* **2022**, *50*, 1957–1961.
26. Lang, P.T.; Bosman, T.; Day, C.; Giegerich, T.; Kircher, M.; Kudlacek, O.; Phillips, G.; Ploeckl, B.; Sieglin, B.; Tretter, J.; et al. Concept for a multi-purpose EU-DEMO pellet launching system. *Fusion Eng. Des.* **2022**, *185*, 113333. [CrossRef]
27. Ohshima, S.; Suzuki, T.; Matoike, R.; Motojima, G.; Kado, S.; Mori, A.; Miyashita, A.; Kobayashi, S.; Minami, T.; Iwata, A.; et al. Three-dimensional dynamics of fluctuations appearing during pellet ablation process around a pellet in a fusion plasma experiment. *Sci. Rep.* **2022**, *12*, 14204. [CrossRef]

28. Zhang, J.; Iwamoto, A.; Shigemori, K.; Hara, M.; Yamanoi, K. Refractive index measurement of hydrogen isotopologue mixture and applicability for homogeneity of hydrogen solid at cryogenic temperature in fusion fuel system. *Nucl. Fusion* **2023**, *63*, 076020. [CrossRef]

29. Gebhart, T.E.; Baylor, L.R.; Dibon, M.; Ericson, M.N.; Felske, E.J.; Frank, S.; Gardner, W.; Ghiozzi, A.G.; Jachmich, S.; Kruezi, U.; et al. Impact of breech geometry and propellant flow on the release of large pellets for the ITER disruption mitigation system. *Nucl. Fusion* **2024**, *64*, 036021. [CrossRef]

30. Mailloux, J.; Abid, N.; Abraham, K.; Abreu, P.; Adabonyan, O.; Adrich, P.; Afanasev, V.; Afzal, M.; Ahlgren, T.; Aho-Mantila, L.; et al. Overview of JET results for optimising ITER operation. *Nucl. Fusion* **2022**, *62*, 042026. [CrossRef]

31. Pavese, F.; Barbero, C. The triple point of pure normal-deuterium. *Cryogenics* **1979**, *19*, 255–260. [CrossRef]

32. Preston-Thomas, H. The International Temperature Scale of 1990 (ITS-90). *Metrologia* **1990**, *27*, 3. [CrossRef]

33. Haynes, W.M. *CRC Handbook of Chemistry and Physics*, 92nd ed.; CRC Press: Boca Raton, FL, USA, 2011.

34. Tegeler, C.; Span, R.; Wagner, W. A New Equation of State for Argon Covering the Fluid Region for Temperatures from the Melting Line to 700 K at Pressures up to 1000 MPa. *J. Phys. Chem. Ref. Data* **1999**, *28*, 779. [CrossRef]

35. Giusepponi, S.; Buonocore, F.; Celino, M.; Pasini, M.L.; Frattolillo, A.; Migliori, S. Study of Solid Molecular Deuterium D2 Growth under Gas Pressure. *Fusion Eng. Des.* **2022**, *182*, 113252. [CrossRef]

36. Thompson, A.P.; Aktulga, H.M.; Berger, R.; Bolintineanu, D.S.; Brown, W.M.; Crozier, P.S.; In't Veld, P.J.; Kohlmeyer, A.; Moore, S.G.; Nguyen, T.D.; et al. LAMMPS—A flexible simulation tool for particle-based materials modeling at the atomic, meso, and continuum scales. *Comp. Phys. Comm.* **2022**, *271*, 10817. [CrossRef]

37. Available online: http://lammps.sandia.gov (accessed on 30 April 2024).

38. Allen, M.P.; Tildesley, D.J. *Computer Simulation of Liquids*; Clarendon Press: Oxford, UK, 1997.

39. Frenkel, D.; Smit, B. *Understanding Molecular Simulation: From Algorithms to Applications*; Academic Press: San Diego, CA, USA, 2002.

40. Haile, J.M. *Molecular Dynamics Simulation: Elementary Methods*; Wiley: New York, NY, USA, 2001.

41. Leach, A. *Molecular Modelling: Principles and Applications*, 2nd ed.; Pren-tice Hall: Harlow, UK, 2001.

42. Rapaport, D.C. *The Art of Molecular Dynamics Simulation*; Cambridge University Press: Cambridge, UK, 2004.

43. Schlick, T. *Molecular Modeling and Simulation*; Springer: Berlin, Germany, 2002.

44. Zepeda-Ruiz, L.A.; Sadigh, B.; Shin, S.J.; Kozioziemski, B.J.; Chernov, A.A. Effect of wetting on nucleation and growth of D2 in confinement. *J. Chem. Phys.* **2018**, *148*, 134708. [CrossRef] [PubMed]

45. Bellissent-Funel, M.C.; Buontempo, U.; Filabozzi, A.; Petrillo, C.; Ricci, F.P. Neutron diffraction of liquid neon and xenon along the coexistence line. *Phys. Rev. B* **1992**, *45*, 4605–4613. [CrossRef]

46. Mick, J.R.; Barhaghi, M.S.; Jackman, B.; Rushaidat, K.; Schwiebert, L.; Potoff, J.J. Optimized Mie potentials for phase equilibria: Application to noble gases and their mixtures with n-alkanes. *J. Chem. Phys.* **2015**, *143*, 114504. [CrossRef]

47. Sadus, R.J. Two-body intermolecular potentials from second virial coefficient properties. *J. Chem. Phys.* **2019**, *150*, 024503. [CrossRef] [PubMed]

48. Deiters, U.K.; Sadus, R.J. Two-body interatomic potentials for He, Ne, Ar, Kr, and Xe from ab initio data. *J. Chem. Phys.* **2019**, *150*, 134504. [CrossRef]

49. Sadus, R.J. Molecular simulation of orthobaric isochoric heat capacities near the critical point. *Phys. Rev. E* **2019**, *99*, 012139. [CrossRef]

50. Deiters, U.K.; Sadus, R.J. Fully a priori prediction of the vapor-liquid equilibria of Ar, Kr, and Xe from ab initio two-body plus three-body interatomic potentials. *J. Chem. Phys.* **2019**, *151*, 034509. [CrossRef]

51. Sadus, R.J. Combining intermolecular potentials for the prediction of fluid properties: Two-body and three-body interactions. *J. Chem. Phys.* **2020**, *153*, 214509. [CrossRef]

52. Sadus, R.J. Effect of the range of particle cohesion on the phase behavior and thermodynamic properties of fluids. *J. Chem. Phys.* **2020**, *153*, 244502. [CrossRef]

53. Deiters, U.K.; Sadus, R.J. Interatomic Interactions Responsible for the Solid–Liquid and Vapor–Liquid Phase Equilibria of Neon. *J. Phys. Chem. B* **2021**, *125*, 8522–8531. [CrossRef]

54. Deiters, U.K.; Sadus, R.J. Accurate determination of solid–liquid equilibria by molecular simulation: Behavior of Ne, Ar, Kr, and Xe from low to high pressures. *J. Chem. Phys.* **2022**, *157*, 204504. [CrossRef]

55. Berendsen, H.J.; Postma, J.V.; Van Gunsteren, W.F.; DiNola, A.R.H.J.; Haak, J.R. Molecular dynamics with coupling to an external bath. *J. Chem. Phys.* **1984**, *81*, 3684. [CrossRef]

56. Curzon, E.; Mascall, A.J. The crystal structures of solid hydrogen and solid deuterium in thin films. *Brit. J. Appl. Phys.* **1965**, *16*, 1301. [CrossRef]

57. Pollack, G.L. The Solid State of Rare Gases. *Rev. Mod. Phys.* **1964**, *36*, 748–791. [CrossRef]

58. Barrett, S.; Meyer, L. X-ray Diffraction Study of Solid Argon. *J. Chem. Phys.* **1964**, *41*, 1078. [CrossRef]

59. Stukowski, A. Computational Analysis Methods in Atomistic Modeling of Crystals. *JOM* **2014**, *66*, 399–407. [CrossRef]

60. Stukowski, A. Structure identification methods for atomistic simulations of crystalline materials. *Model. Simul. Mater. Sci. Eng.* **2012**, *20*, 045021. [CrossRef]

61. Iannone, F.; Ambrosino, F.; Bracco, G.; De Rosa, M.; Funel, A.; Guarnieri, G.; Migliori, S.; Palombi, F.; Ponti, G.; Santomauro, G.; et al. CRESCO ENEA HPC clusters: A working example of a multifabric GPFS Spectrum Scale layout. In Proceedings of the 2019 International Conference on High Performance Computing & Simulation (HPCS), Dublin, Ireland, 15–19 July 2019; pp. 1051–1052.
62. Mariano, A.; D'amato, G.; Ambrosino, F.; Aprea, G.; Buonocore, F.; Celino, M.; Colavincenzo, A.; Fina, M.; Funel, A.; Giusepponi, S.; et al. Fast Access to Remote Objects 2.0 a renewed gateway to ENEAGRID distributed computing resources. *Futur. Gener. Comput. Syst.* **2019**, *94*, 920–928. [CrossRef]